





Cite this: DOI: 10.1039/d0nr04884d

# Methanol-derived high-performance $\text{Na}_3\text{V}_2(\text{PO}_4)_3/\text{C}$ : from kilogram-scale synthesis to pouch cell safety detection†

 Yuqiang Pi,<sup>a</sup> Zhiwei Gan,<sup>a</sup> Zheng Li,<sup>b</sup> Yushan Ruan,<sup>a</sup> Cunyuan Pei,<sup>a</sup> Hui Yu,<sup>a</sup> Kang Han,<sup>a</sup> Yaowen Ge,<sup>b</sup> Qinyou An <sup>\*a,c</sup> and Liqiang Mai <sup>\*a,c</sup>

$\text{Na}_3\text{V}_2(\text{PO}_4)_3$  (NVP) is regarded as a potential cathode material that can be applied in sodium ion batteries (SIBs) owing to its NASICON structure. However, most of the reported works have focused on the synthesis of materials and the improvement of their electrochemical properties, with little research on the design and safety of pouch cells. Herein, we implemented a cost-saving route to realize the industrial-scale synthesis of NVP cathode materials. The obtained NVP samples possess an impressive Na-ion storage capability with high reversible capacity ( $116.3 \text{ mA h g}^{-1}$  at 0.2 C), superior power capability ( $97.9 \text{ mA h g}^{-1}$  at 30 C), and long lifespan (71.6% capacity retention after 2500 cycles at 20 C). It was remarkable that industrial-scale NVP/hard carbon (HC) sodium-ion pouch cells could be designed with an 823 mA h discharge capacity at a current of 200 mA (about 0.25 C), and which possess a long life and high rate performance (1000 cycles with a little decay at a current of 4000 mA). Besides, the pouch cells also exhibit excellent thermal stability when demonstrated for application in unmanned aerial vehicles (UAVs), and puncturing experiment results can further prove the excellent safety performance of NVP-hard carbon pouch cells.

 Received 29th June 2020,  
Accepted 26th August 2020

DOI: 10.1039/d0nr04884d

[rsc.li/nanoscale](http://rsc.li/nanoscale)

## Introduction

For decades, the market in portable electronic energy storage devices has been dominated by Li-ion batteries (LIBs), which is attributable to their advantages of high energy or power density with long cycling life.<sup>1,2</sup> However, the high cost and limited sources of Li seriously hinder the development of LIBs on to a larger scale, for example, grid-scale energy storage systems (ESSs).<sup>3,4</sup> However, there are a few critical factors for stationary batteries applied in ESSs, such as low self-discharge behavior, superior rate performance, and stable operation state in any climate and chemistry.<sup>5</sup> Alternatively, sodium-ion batteries (SIBs) have been studied for years as a promising technology beyond being a counterpart to the LIBs, mainly ascribed to the higher abundance of sodium sources compared with those of lithium and sodium's similar electro-

chemical intercalation behavior as that of Li.<sup>6–13</sup> Besides, the production line for manufacturing LIBs can be applied directly to assemble SIBs, and thus avoid wasting of production resources. Inspired by these advantageous conditions, extensive efforts have been devoted to studying electrode materials, electrolytes, and full-cell structure design of SIBs aimed at promoting SIBs for commercialization. However, on account of the larger ionic radius of sodium, there exist some issues about the low  $\text{Na}^+$  diffusion coefficient into the electrode and structure degradation during  $\text{Na}^+$  intercalation/de-intercalation, which leads to the inferior power capability and cyclic ability of SIBs.<sup>14–16</sup> Therefore, the search for applicable electrode materials with stable structure and fast ion diffusion pathways is becoming the key factor in the development of SIBs.

As a cathode material with typical sodium super-ionic conductor (NASICON) structure,  $\text{Na}_3\text{V}_2(\text{PO}_4)_3$  (NVP) has received extensive attention by reason of its 3-D open frameworks, providing fast Na-ion transport pathways and maintaining structural stability. So far, a wide variety of synthetic routes has been attempted to investigate the Na-ion storage performance of NVP, such as the high-energy ball milling method, sol-gel method, and spray-drying method. Park *et al.*<sup>17</sup> synthesized a 3D interconnected porous structure of NVP by adopting a modified sol-gel method; the NVP@C possessed high dis-

<sup>a</sup>State Key Laboratory of Advanced Technology for Materials Synthesis and Processing, Wuhan University of Technology, Wuhan 430070, Hubei, China.  
E-mail: mlq518@whut.edu.cn, anqinyou86@whut.edu.cn

<sup>b</sup>WUT Powerful Energy Co., Ltd, Wuhan 430223, Hubei, China

<sup>c</sup>Foshan Xianhu Laboratory of the Advanced Energy Science and Technology Guangdong Laboratory, Foshan 528200, Guangdong, China

†Electronic supplementary information (ESI) available. See DOI: 10.1039/d0nr04884d

charge specific capacity, attaining  $116.9 \text{ mA h g}^{-1}$  at 1 C. Sun *et al.*<sup>18</sup> implemented a high-energy ball milling route to obtain the off-stoichiometric  $\text{Na}_{3-3x}\text{V}_{2+x}(\text{PO}_4)_3$ , which still delivered 79% of the theoretical capacity (about  $117 \text{ mA h g}^{-1}$ ) at 20 C. Our group<sup>19</sup> reported a simple self-sacrificed method to prepare a 3-D NVP nanofiber network with 95.9% capacity retention over 1000 cycles at 10 C. However, most reported methods are only suitable for synthesizing electrode materials in the laboratory scale with output of only a few grams. If we wish to scale up output to industrial quantities (kilogram-class), many key factors of the synthetic methods above, such as production efficiency, consistency of products, and manufacturing cost, will limit NVP from being used in electrode material production. Among the multitudinous synthetic routes, spray-drying has been demonstrated to be one of the most appropriate methods to prepare electrode materials for LIBs and SIBs in upscaling to industrial quantities,<sup>20</sup> owing to the synthesis of homogeneous electrode materials with high tap density and reproducible results. To our knowledge,  $\text{LiFePO}_4$ ,<sup>21-25</sup>  $\text{Li}_4\text{Ti}_5\text{O}_{12}$ ,<sup>26-28</sup>  $\text{Li}_3\text{V}_2(\text{PO}_4)_3$ ,<sup>29-31</sup>  $\text{NaTi}_2(\text{PO}_4)_3$ ,<sup>32,33</sup>  $\text{Na}_2\text{MnPO}_4\text{F}$ ,<sup>34,35</sup> and  $\text{V}_2\text{O}_5$ <sup>36</sup> have been obtained by the spray-drying route and applied in LIBs or SIBs fields.

It is well known that LIBs are making life convenient to human beings. However, in recent years, there have been many safety accidents with LIBs, which sent out a signal for us to attach great importance to battery safety. Taking into account the many factors in safety accidents with LIBs, thermal runaway of cells is the most vital one, which can give rise to fire and/or explosion.<sup>37-39</sup> As well as LIBs, more attention must be paid to concerns about safety and reliability of SIBs. Many methods have been introduced for evaluating the abuse tolerance of lithium- or sodium-ion batteries, including short-circuiting, overcharging, oven test, puncturing test, crushing test and so on.<sup>40,41</sup> The puncturing test is conducted by forcing a nail through the battery. As the test is going on, a large amount of heat accumulates in a short period of time and arouses the thermal runaway, which is mainly caused by the internal short-circuiting of the battery. In general, the hazard of thermal runaway in a single cell is extremely low. Yet if the thermal runaway appears in hundreds of cells packed together, the consequences of fire and/or explosion are unimaginable. It is worth noting that the whole battery system could be destroyed by the cell-to-cell spread of the thermal runaway, if it happens in a single cell.<sup>42</sup> Therefore, research into SIBs should focus on not only battery material technology but also battery safety.

Herein, we developed an industrialized spray-drying route to realize  $\text{Na}_3\text{V}_2(\text{PO}_4)_3$  in industrialized amplification (kilogram-class). The obtained  $\text{Na}_3\text{V}_2(\text{PO}_4)_3$  samples exhibit outstanding Na-ion storage capability with high reversible capacity, superior power capability, and long cycling life. Furthermore, we designed  $\text{Na}_3\text{V}_2(\text{PO}_4)_3$ -hard carbon Na-ion pouch cells, and the pouch cells could deliver an  $823 \text{ mA h}$  discharge capacity at a current of 200 mA (about 0.25 C), and display a long life at an extremely high current of 4000 mA (about 5 C) for over 1000 cycles. Besides, the unmanned aerial

vehicle (UAV) demonstration and puncturing experiment were also carried out to prove the thermal stability and safety performance of NVP-hard carbon pouch cells.

## Experimental

### Synthetic procedures

M-NVP/C microspheres could be obtained through a spray-drying and subsequent calcination route. In a typical procedure illustrated in Fig. 1, 1.685 kg of  $\text{NaH}_2\text{PO}_4$ , 0.654 kg of  $\text{V}_2\text{O}_5$ , 0.4 kg of  $\text{C}_6\text{H}_{12}\text{O}_6 \cdot \text{H}_2\text{O}$  and 15 L of methanol were fed into a ball milling tank with Zr balls and then continually mixed for 2 h. After being mixed uniformly, the obtained slurry was spray-dried at  $205 \text{ }^\circ\text{C}$  to form a solid precursor, then calcinated in  $\text{N}_2$  atmosphere at  $800 \text{ }^\circ\text{C}$  with a heating rate of  $2 \text{ }^\circ\text{C min}^{-1}$  and maintained for 8 h. Finally, carbon-coated  $\text{Na}_3\text{V}_2(\text{PO}_4)_3$  microsphere samples were obtained and weighed about 1200 g, as described in Fig. S1.† However, more than 400 g of product was lost during the whole preparation process, mainly as a result of losing the intermediate product bonded to the wall of the spray dryer. Fig. 1 summarizes the specific procedure route for feeding, mixing, spray-drying, calcinating, and obtaining the product. For H-NVP/C, methanol was replaced by distilled water.

### Materials and methods

The crystallographic information of the final products was analyzed with a D8 Advance X-ray diffractometer (XRD) with a non-monochromated  $\text{Cu K}\alpha$  X-ray source. Raman measurement was performed to investigate the nature of the carbon layer and hard carbon with a Renishaw INVIA micro-Raman spectroscopy system. Information on the morphology was obtained through JEOL-7100F microscopy. Transmission electron microscopy (TEM) and high-resolution transmission electron microscopy (HRTEM) images were recorded with a JEM-2100F microscope. A Tristar II 3020 instrument was used to measure the BET surface areas by nitrogen adsorption at 77 K. TG-DSC analysis was performed using a NETZSCH-STA449c/3/G thermoanalyzer. The value of tap density was got using a BT-300 instrument. Carbon contents

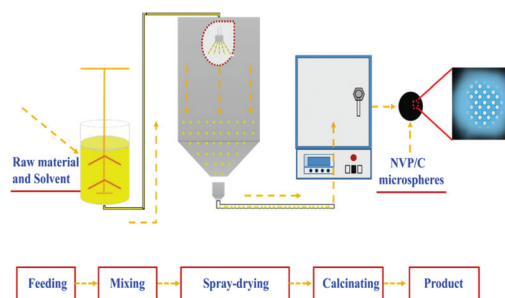


Fig. 1 Schematic illustration of the typical synthetic route of NVP/C microspheres.

were determined using a Vario EL cube CHNSO elemental analyzer.

### Electrochemical characterizations

The electrochemical performances of Na-ion half cells assembled with 2016 coin cells in a glove box full of pure argon gas are demonstrated based on the following method. Na metal served as the anode, the electrolyte was made by compounding 1 M solution of NaClO<sub>4</sub> into ethylene carbon (EC)–dimethyl carbonate (DMC) (1 : 1 w/w) and 5% FEC, and a Whatman glass Micro-fibre Filter (Grade GF/F) acted as the separator. The mixture of 80 wt% active materials, 10 wt% carbon nanotube conductive paste, and 10 wt% PVDF with a proper amount of *N*-methyl-2-pyrrolidone (NMP) solvent was coated on an Al foil to form the cathode electrode and dried in a vacuum oven for 24 h at 105 °C. Then, the electrode was cut into circular pieces of 14 mm diameter with about 1.5–2.0 mg cm<sup>-2</sup> of the mass loading of active materials. A battery test system (LAND CT2001A) was employed for carrying out the galvanostatic charge–discharge tests, where 1 C is equal to 117 mA h g<sup>-1</sup>. A CHI 760e electrochemical workstation was used for performing the cyclic voltammetry (CV) and electrochemical impedance spectroscopy (EIS) tests.

Pouch cells were fabricated to verify the Na-ion storage capability of the NVP cathode material. An aluminum-plastic film served as the sealing. A 1 M solution of NaClO<sub>4</sub> in ethylene carbon (EC)–dimethyl carbonate (DMC) (1 : 1 w/w) and 2% FEC were used as the electrolyte, and the separator applied in lithium-ion batteries can be also used for fabricating sodium-ion pouch cells. The mixture of 90.5 wt% active material, 1.5 wt% carbon nanotube conductive paste, 2 wt% carbon black, 6 wt% PVDF, and a proper amount of *N*-methyl-2-pyrrolidone (NMP) was put into a planetary mixer to form a uniform cathode slurry with an appropriate viscosity, which was then coated on an Al foil afterwards. The electronic images of the NVP cathode pole pieces with 10–11 mg cm<sup>-2</sup> of surface mass density are shown in Fig. S2a and b.† The anode slurry was coated on a Cu foil made of 93.8 wt% hard carbon (HC), 2 wt% carbon black, 1.7 wt% sodium carboxymethyl cellulose (CMC), 2.5 wt% styrene butadiene rubber (SBR) and the right amount of distilled water. The surface mass density of the HC anode is 3–3.5 mg cm<sup>-2</sup>. The electronic images of the HC anode pole pieces are displayed in Fig. S2c and d.† All the electrode pieces were kept in a vacuum oven at 110 °C until the water content in them was less than 500 ppm. The capacity test for Na-ion pouch cells was conducted with a battery test system (TITANS THCX-IO/5-96-M-A).

## Results and discussion

Fig. 2a presents the XRD patterns of the M-NVP/C and H-NVP/C samples. All the diffraction peaks are well indexed to the rhombohedral NVP (JCPDS no. 53-0018), in accordance with previous reports.<sup>19,43,44</sup> As is clear in Fig. 2b, the Raman spectra of M-NVP/C and H-NVP/C possess two characteristic

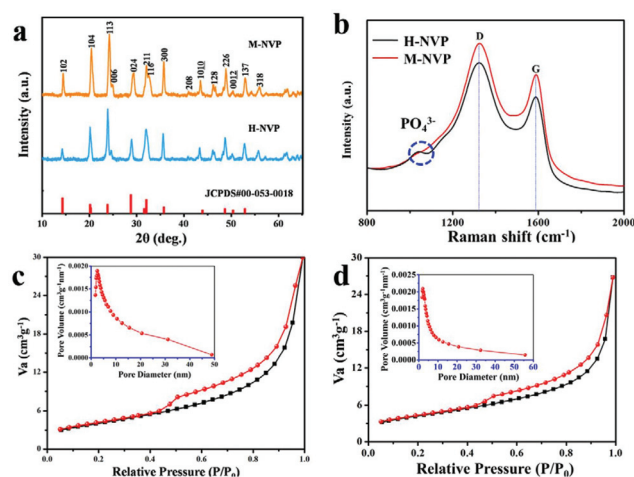
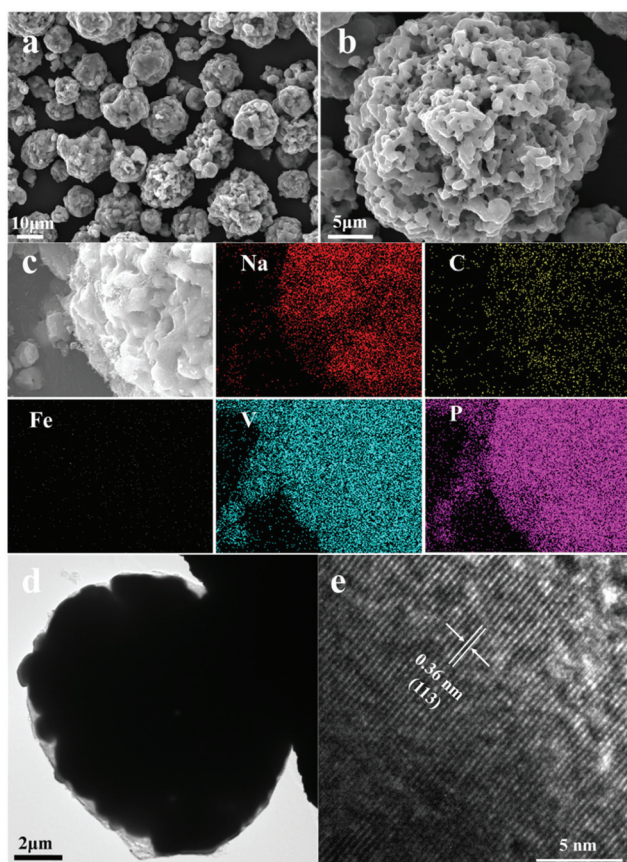


Fig. 2 (a) XRD patterns of M-NVP/C and H-NVP/C; (b) Raman spectra of M-NVP/C and H-NVP/C; (c) nitrogen adsorption–desorption isotherms and corresponding pore size distributions (inset) of M-NVP/C (c) and H-NVP/C (d).

bands appearing at 1326 cm<sup>-1</sup> and 1590 cm<sup>-1</sup>, which are identified as the D-band (disordered carbon) and G-band (crystalline graphitized carbon), respectively. The intensity ratios ( $I_D/I_G$ ) for M-NVP/C and H-NVP/C samples are about 1.23 and 1.30, respectively, suggesting that the M-NVP/C samples possess a higher degree of graphitization. Besides, there is a band appearing at around 1000 cm<sup>-1</sup> in the H-NVP/C sample, which was caused by the stretching vibrations of PO<sub>4</sub>.<sup>44,45</sup> Moreover, CHNSO elemental analysis was conducted for measuring the carbon content. It is known that the amorphous carbon content of M-NVP/C is 3 wt%, slightly higher than 2.7 wt% for H-NVP/C, and the similar result can be confirmed by the TGA test (Fig. S3†). This phenomenon can be explained as the different ball-milling solvents result in different degrees of graphitization and carbon content. BET measurement was conducted to determine the surface area and pore-size distribution of M-NVP/C (Fig. 2c) and H-NVP/C (Fig. 2d). The BET specific surface areas are 14.9 and 15.2 m<sup>2</sup> g<sup>-1</sup> for M-NVP/C and H-NVP/C samples, respectively, with a pore diameter of 1–5 nm, demonstrating the voids and inter-spaces of microspheres to relieve the internal stress of the structure.

The electronic images of the precursor and product in the mullite saggars are presented in Fig. S4a and b.† It is found that the colours of the precursor and final products are dark green and pure black, respectively. The morphology of M-NVP/C is shown in Fig. 3a and b. Microspheres with size of around 10–20 μm are successfully obtained by the spray-drying route. The SEM images show that the microspheres consist of numerous intercalated nanoparticles, which leads to plenty of voids. The structure is useful in providing fast Na-ion diffusion pathways, enlarged electrode–electrolyte contact areas, and relieving of internal stress. The similar microsphere structure found in the H-NVP/C sample is illustrated in Fig. S5a and b.† The result of EDS indicates that Na, C, V, and P are distributed uni-



**Fig. 3** (a and b) SEM images of M-NVP/C; (c) is the corresponding EDS elemental mapping; (d) TEM and (e) HRTEM images of M-NVP/C.

formly. The presence of elemental Fe in the M-NVP/C (Fig. 3c) and H-NVP/C (Fig. S5c†) samples was unexpected, which is mainly attributed to equipment wear and tear. According to the result from inductive coupled plasma emission spectrometer (ICP), the content of Fe is very low, about 0.3%. Moreover, the amorphous carbon coating layer on the surface of the particles could be observed clearly on the TEM images (Fig. 3d and S5d†). The lattice fringes of M-NVP/C (Fig. 3e) and H-NVP/C (Fig. S5e†) with  $d$ -spacings of about 0.36 nm and 0.44 nm could be clearly observed, originating from the (113) and (104) planes of NVP, respectively. Tap density was evaluated with a vibration density meter. The value of tap density for M-NVP/C is about 0.9–0.95 g mL<sup>-1</sup>, which is much higher than that for NVP nanostructures previously published. It is well known that high tap density could provide higher gravimetric and volumetric energy densities and is beneficial for commercializing the cathode material and SIBs.<sup>46</sup>

Fig. 4 shows the comparison between the Na-ion storage capability in half cells between M-NVP/C and H-NVP/C samples in the potential range of 2.2–3.8 V. The CV test (Fig. 4a) was performed at a scan rate of 0.1 mV s<sup>-1</sup>. As is known to all, the redox peaks of NVP in the range of 2.2–3.8 V correspond to the reversible V<sup>3+</sup>/V<sup>4+</sup> redox couple reaction. Remarkably, there is a split at around 3.2 V of reduction peaks,

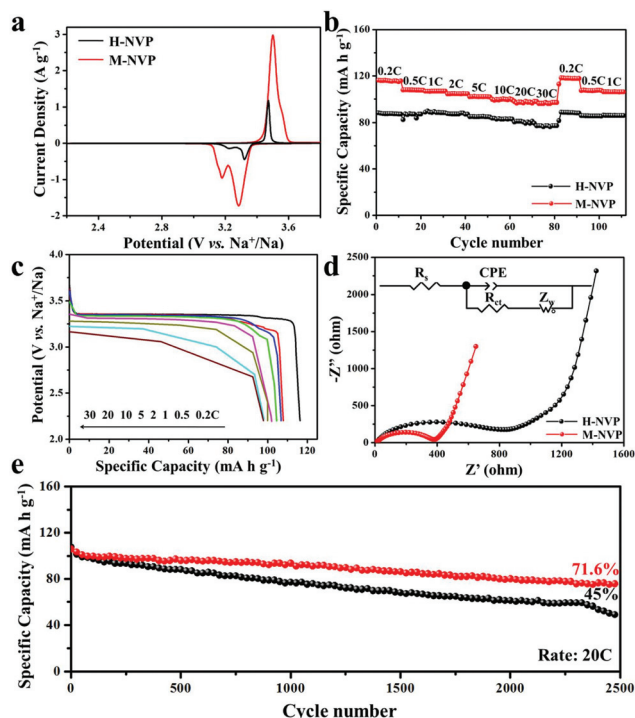


**Fig. 4** Na-ion storage capability of M-NVP/C and H-NVP/C in half cells with a potential range from 2.2 to 3.8 V; (a) the CV curves of M-NVP/C and H-NVP/C at a scan rate of 0.1 mV s<sup>-1</sup>; (b) rate performance of the M-NVP/C and H-NVP/C electrodes; (c) galvanostatic discharge curves of M-NVP/C at varied current rates from 0.2 C to 30 C; (d) the Nyquist plots of M-NVP/C and H-NVP/C after 2500 cycles at 20 C with an equivalent circuit inset; (e) cyclic capability of M-NVP/C and H-NVP/C at 20 C.

which mainly arises from the structural rearrangement happening to Na-ion migration from Na(1) to the Na(2) sites in the NASICON framework.<sup>43,47</sup> The rate performances of the M-NVP/C and H-NVP/C are shown in Fig. 4b. Apparently, compared with H-NVP/C, the M-NVP/C sample possesses higher discharge capacity under each current rate, showing improved rate capability. According to Fig. 4c, it is known that the M-NVP/C electrode can deliver reversible capacities as high as 116.3, 107.9, 106.7, 104.5, 102, 99.9, 98.1, and 97.9 mA h g<sup>-1</sup> at current rates of 0.2, 0.5, 1, 2, 5, 10, 20, and 30 C, respectively. Then, when the current density is back to 0.2 C, the capacity of 118.3 mA h g<sup>-1</sup> could be achieved without any decay. To evaluate the cycling life span of the two samples, a high current rate of 20 C is adopted and cycling for over 2500 cycles. As shown in Fig. 4e, M-NVP/C and H-NVP/C could deliver the initial specific capacity of 105.7 and 107.6 mA h g<sup>-1</sup>, respectively. After 2500 cycles, M-NVP/C can still maintain 71.6% of the initial capacity, attaining 75.7 mA h g<sup>-1</sup>, indicating an impressive cycling life span with an excellent material power density. For comparison, H-NVP/C could only achieve a capacity of 48.3 mA h g<sup>-1</sup> with a 45% capacity retention. Then, we conducted the electrochemical impedance spectroscopy (EIS) test with the half cells after testing the long-term cyclability of M-NVP/C and H-NVP/C, recorded in Fig. 4d. The value of  $R_{ct}$

(charge transfer resistance) for the M-NVP/C electrode is 381  $\Omega$ , far smaller than that for H-NVP/C (830  $\Omega$ ), indicating the changeability of charge transfer kinetics by mixing a different solvent. According to the results of Raman measurement and electrochemical characterization, it is demonstrated that methanol as the mixing solvent can effectively improve the electronic conductivity of NVP cathode material, which may be attributed to the tribological effects in methanol. The activation energy of pyrolytic carbon milled in the methanol environment, other than milled in the water environment, could be reduced due to the increased friction effect; that is, a higher degree of graphitization and electric conductivity can be obtained for the coated carbon, owing to the reduced activation energy under the same calcinating temperature.

Among numerous anode materials used in SIBs,<sup>48–51</sup> hard carbon has been researched for many years. Therefore, in our work, commercialized hard carbon is also used for verifying the excellent Na-ion storage performance of the M-NVP/C electrode. The Raman spectra (Fig. S6a†) of hard carbon exhibit a broad D-band (around 1344  $\text{cm}^{-1}$ ) and a G-band (around 1593  $\text{cm}^{-1}$ ). The  $I_D/I_G$  for HC (hard carbon) is about 1.014. The morphology of HC is displayed in Fig. S6b,† where the block-shaped particles with diameters of around 5–10  $\mu\text{m}$  can be observed. Fig. S7a† shows the CV curves of HC at a scan rate of 0.1  $\text{mV s}^{-1}$  in the potential range of 0.01–2 V. There is a pair of redox peaks appearing at about 0.1 V in HC electrodes, which can be ascribed to the sodium insertion/extraction into/from the hard carbon material. However, the initial coulombic efficiency of hard carbon is relatively low, limiting the wide application of sodium ion batteries. As illustrated in Fig. S7b,† coulombic efficiencies of 61.6% 56.1% 50.9% and 42.4% could be achieved for HC at the current densities of 50, 100, 200 and 300  $\text{mA g}^{-1}$ , respectively, which is much against operating the capacity of the cells. Fig. S7c† shows the cycling ability of HC at different current densities. Apparently, there is no decay in specific capacity after 100 cycles at each current density, which indicates the outstanding cyclability of hard carbon.

Na-ion full cells containing M-NVP/C and hard carbon were designed and fabricated. Fig. 5a shows the CV curves of full cells characterized by an assembly of 2016 coin cells at a scanning rate of 0.1  $\text{mV s}^{-1}$  in the potential range of 2.2–3.65 V. It is evident that a pair of redox peaks appears in relation to the reversible  $\text{V}^{3+}/\text{V}^{4+}$  redox couple reaction. Fig. 5b displays the discharge curves of pouch cells kept under different test temperatures and discharged at the current of 200 mA (about 0.25 C). At room temperature (25  $^{\circ}\text{C}$ ), pouch cells could achieve the capacity of 832 mA h. As the testing temperature was changed, the cells displayed separately the capacity of 632.3 624.8, and 247.9 mA h at the temperature of 60  $^{\circ}\text{C}$ ,  $-20^{\circ}\text{C}$ , and  $-40^{\circ}\text{C}$ , and about 76%, 75.1%, and 29.8% of the capacity at room temperature is maintained, respectively. The long-term cyclability of the Na-ion pouch cells containing M-NVP/C and hard carbon is shown in Fig. 5c. At the discharge currents of 500, 1000, and 4000 mA, Na-ion full cells deliver the discharging capacities of 621.1, 681.4, and 487.6 mA h for the first cycle, respectively. The discharging capacities present a trend

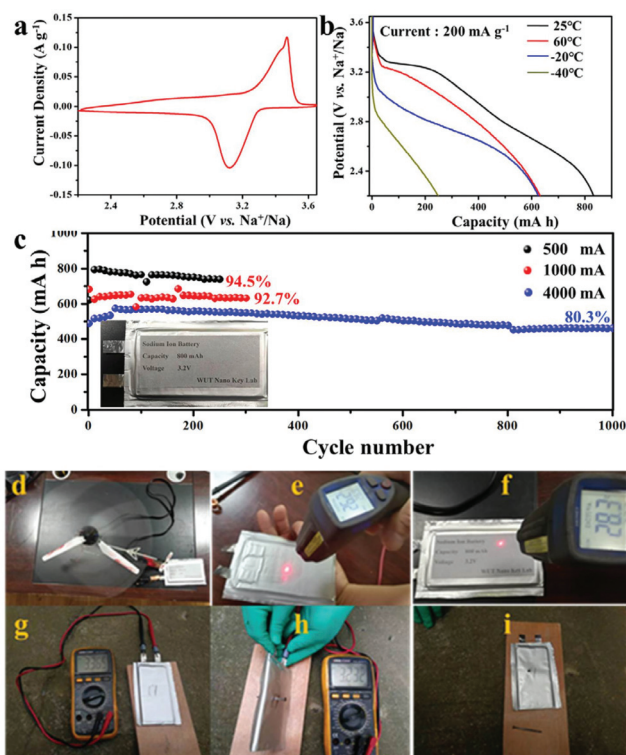


**Fig. 5** (a) The CV curve of Na-ion full cell characterized by an assembly of 2016 coin cells at a scanning rate of 0.1  $\text{mV s}^{-1}$  in the potential range of 2.2–3.65 V; (b) galvanostatic discharge curves of Na-ion pouch cells kept under different temperatures from 60  $^{\circ}\text{C}$  to  $-40^{\circ}\text{C}$  at the discharge current of 200 mA; (c) cycling performance of Na-ion full cells at varied currents from 500 mA to 4000 mA; (d) image of a working UAV combined with sodium-ion full batteries; (e and f) surface temperatures of the cell before and after operating the UAV, respectively; and (g, h and i) images of sodium-ion full batteries undergoing the puncturing test.

of rising and then declining, which is ascribed to the electrochemical activation of the electrode. With the cycle number increasing, highest discharging capacities of 798.3, 683.7 and 575.1 mA h are reached subsequently. Herein  $C_T$  refers to the termination discharge capacities. So, the numerical value of  $100 \times C_T/C_H$  ( $C_H$ , the highest discharging capacities) can be used to characterize the long-term cyclability of the Na-ion full cells. The values are 92.5%, 92.4%, and 80.3% at currents of 500, 1000, and 4000 mA after 250, 300, and 1000 cycles, respectively. It is worth noting that the power density of pouch cells cycled at the current of 4000 mA can reach as high as 320  $\text{W L}^{-1}$ , demonstrating that NVP/HC Na-ion full batteries possess excellent power capability.

Herein the Na-ion pouch cells were put into practical application for unmanned aerial vehicles (UAVs). As a UAV was connected with prepared batteries, a pair of airscrews rotated quickly (Fig. 5d). Using a multimeter for the operating-current test, the numerical value is about 5.5 A. With airscrews rotating, the voltage of the cell slowly dropped to 2.2 V. The rotating time we counted was nearly 7 min. During the whole operating process, the cell showed high stability without gas expansion or size change. Fig. 5e and f show the surface temperature of

the cell before and after operating the UAV, respectively—26.2 °C is the surface temperature of cell before, and 28.3 °C after operating—which demonstrates the excellent thermal stability and power performance of Na-ion pouch cells containing M-NVP/C and hard carbon. Moreover, the puncturing method was carried out to determine the safety of the prepared Na-ion full cells. The cell maintained a 100% charging state in Fig. 5g. Fig. 5h shows the process of puncturing the nail into the cell. The process of pulling out the nail from the cell is shown in Fig. 5i. It is evident that there is no phenomenon of firing, smoking or exploding, proving that the Na-ion full cells have excellent safety performance.

## Conclusions

In summary, an industrialized spray-drying route was developed to realize industrial-scale synthesis of NVP cathode materials. It is proved that adopting methanol as the mixing solvent results in superior tap density and higher degrees of graphitization and carbon content of NVP/C. The M-NVP/C microspheres consist of interconnected nanoparticles, which can provide sufficient pores or channels for Na<sup>+</sup> transport, enlarge electrode–electrolyte contact area, and relieve the internal stress of the microsphere structure. The obtained NVP samples display outstanding Na-ion storage capability with a high reversible capacity (116.3 mA h g<sup>-1</sup> at 0.2 C), excellent power capability (97.9 mA h g<sup>-1</sup> at 30 C), and a long life span (71.6% capacity retention after 2500 cycles at 20 C). It is remarkable that NVP-hard carbon (HC) sodium-ion pouch cells could be designed with an 823 mA h discharge capacity at a current of 200 mA (about 0.25 C), and they display a long life and high rate (1000 cycles with a little decay at the current of 4000 mA). Besides, the pouch cells also exhibit excellent thermal stability when they were demonstrated for application in unmanned aerial vehicles (UAVs), and puncturing experiment results further proved the excellent safety performance of the NVP-hard carbon pouch cells.

## Conflicts of interest

There are no conflicts to declare.

## Acknowledgements

This work was supported by the Natural Science Foundation of Hubei Province (2019CFA001), the National Natural Science Foundation of China (51832004, 51521001), the National Key Research and Development Program of China (2016YFA0202603), and Foshan Xianhu Laboratory of the Advanced Energy Science and Technology Guangdong Laboratory (XHT2020-003).

## Notes and references

- J. Liu, *Adv. Funct. Mater.*, 2013, **23**, 924–928.
- Z. Yang, J. Zhang, M. W. Kintner-Meyer, X. Lu, D. W. Choi, J. P. Lemmon and J. Liu, *Chem. Rev.*, 2011, **111**, 3577–3613.
- N. S. Choi, Z. Chen, S. A. Freunberger, X. Ji, Y. K. Sun, K. Amine, G. Yushin, L. F. Nazar, J. Cho and P. G. Bruce, *Angew. Chem., Int. Ed.*, 2012, **51**, 9994–10024.
- H. Zhou, *Energy Environ. Sci.*, 2013, **6**, 2256–2256.
- T. Liu, Y. Zhang, Z. Jiang, X. Zeng, J. Ji, Z. Li, X. Gao, M. Sun, Z. Lin, M. Ling, J. Zheng and C. Liang, *Energy Environ. Sci.*, 2019, **12**, 1512–1533.
- M. Li, Z. Du, M. A. Khaleel and I. Belharouak, *Energy Storage Mater.*, 2020, **25**, 520–536.
- L. Zhou, K. Zhang, Z. Hu, Z. Tao, L. Mai, Y. Kang, S. Chou and J. Chen, *Adv. Energy Mater.*, 2018, **8**, 1701415.
- J. Deng, W. Luo, S. Chou, H. Liu and S. Dou, *Adv. Energy Mater.*, 2018, **8**, 1701428.
- W. Ren, Z. Zhu, Q. An and L. Mai, *Small*, 2017, **13**, 1604181.
- N. Yabuuchi, K. Kubota, M. Dahbi and S. Komaba, *Chem. Rev.*, 2014, **114**, 11636–11682.
- P. Xiong, F. Zhang, X. Zhang, S. Wang, H. Liu, B. Sun, J. Zhang, Y. Sun, R. Ma, Y. Bando, C. Zhou, Z. Liu, T. Sasaki and G. Wang, *Nat. Commun.*, 2020, **11**, 3297.
- Z. Liu, J. Wang and B. Lu, *Sci. Bull.*, 2020, **65**, 1242–1251.
- Z. Liu, J. Wang, H. Ding, S. Chen, X. Yu and B. Lu, *ACS Nano*, 2018, **12**, 8456–8466.
- S. Li, Y. Dong, L. Xu, X. Xu, L. He and L. Mai, *Adv. Mater.*, 2014, **26**, 3545–3553.
- S. P. Ong, V. L. Chevrier, G. Hautier, A. Jain, C. Moore, S. Kim, X. Ma and G. Ceder, *Energy Environ. Sci.*, 2011, **4**, 3680–3688.
- Y. Cai, X. Cao, Z. Luo, G. Fang, F. Liu, J. Zhou, A. Pan and S. Liang, *Adv. Sci.*, 2018, **5**.
- P. N. Didwal, R. Verma, C. W. Min and C. J. Park, *J. Power Sources*, 2019, **413**, 1–10.
- P. Sun, Y. Wang, X. Wang, Q. Xu, Q. Fan and Y. Sun, *RSC Adv.*, 2018, **8**, 20319–20326.
- W. Ren, Z. Zheng, C. Xu, C. Niu, Q. Wei, Q. An, K. Zhao, M. Yan, M. Qin and L. Mai, *Nano Energy*, 2016, **25**, 145–153.
- B. Vertruyen, N. Eshraghi, C. Piffet, J. Bodart, A. Mahmoud and F. Boschini, *Materials*, 2018, **11**, 1076.
- J. Sun, Z. Li, X. Ren, L. Wang and G. Liang, *J. Alloys Compd.*, 2019, **773**, 788–795.
- H. Liu, Y. Liu, L. An, X. Zhao, L. Wang and G. Liang, *J. Electrochem. Soc.*, 2017, **164**, A3666–A3672.
- Q. Liu, S. Liao, H. Song and Z. Liang, *J. Power Sources*, 2012, **211**, 52–58.
- F. Yu, J. Zhang, Y. Yang and G. Song, *J. Mater. Chem.*, 2009, **19**, 9121–9125.
- Y. Yan, Q. Li, B. Ren, R. Yang, Y. Xu, L. Zhong and H. Wu, *Ionics*, 2018, **24**, 671–679.
- C. W. Chang-jian, E. C. Cho, J. H. Huang, J. H. Huang, J. A. Chou, B. C. Ho, K. C. Lee and Y. S. Hsiao, *J. Alloys Compd.*, 2019, **773**, 376–386.

- 27 D. Ruan, M. S. Kim, B. Yang, J. Qin, K. B. Kim, S. H. Lee, Q. Liu, L. Tan and Z. Qiao, *J. Power Sources*, 2017, **366**, 200–206.
- 28 P. K. Alaboina, Y. Ge, M. J. Uddin, Y. Liu, D. Lee, S. Park, X. Zhang and S. J. Cho, *ACS Appl. Mater. Interfaces*, 2016, **8**, 12127–12133.
- 29 Y. Li, J. Wang, Z. Zhou, J. Deng, Q. Yao, H. Chu, Z. Wang, L. Sun and H. Zhou, *J. Alloys Compd.*, 2019, **774**, 879–886.
- 30 Y. Hu, X. Ma, P. Guo, F. Jaeger and Z. Wang, *J. Alloys Compd.*, 2017, **723**, 873–879.
- 31 L. Wu, S. Zhong, J. Lu, F. Lv and J. Liu, *Mater. Lett.*, 2014, **115**, 60–63.
- 32 H. Liu, H. Zhang, C. Su, X. Li and Y. Guo, *Solid State Ionics*, 2018, **322**, 79–84.
- 33 Y. Fang, L. Xiao, J. Qian, Y. Cao, X. Ai, Y. Huang and H. Yang, *Adv. Energy Mater.*, 2016, **6**, 1502197.
- 34 L. Wu, Y. Hu, X. Zhang, J. Liu, X. Zhu and S. Zhong, *J. Power Sources*, 2018, **374**, 40–47.
- 35 X. Lin, X. Hou, X. Wu, S. Wang, M. Gao and Y. Yang, *RSC Adv.*, 2014, **4**, 40985–40993.
- 36 X. Jia, L. Zhang, R. Zhang, Y. Lu and F. Wei, *RSC Adv.*, 2014, **4**, 21018–21022.
- 37 D. P. Finegan, M. Scheel, J. B. Robinson, B. Tjaden, M. Di Michiel, G. Hinds, D. J. L. Brett and P. R. Shearing, *Phys. Chem. Chem. Phys.*, 2016, **18**, 30912–30919.
- 38 D. P. Finegan, M. Scheel, J. B. Robinson, B. Tjaden, I. Hunt, T. J. Mason, J. Millichamp, M. Di Michiel, G. J. Offer, G. Hinds, D. J. L. Brett and P. R. Shearing, *Nat. Commun.*, 2015, **6**, 6924.
- 39 D. P. Finegan, E. Darcy, M. Keyser, B. Tjaden, T. M. M. Heenan, R. Jervis, J. J. Bailey, N. T. Vo, O. V. Magdysyuk, M. Drakopoulos, M. Di Michiel, A. Rack, G. Hinds, D. J. L. Brett and P. R. Shearing, *Adv. Sci.*, 2018, **5**, 1700369.
- 40 Q. Wang, P. Ping, X. Zhao, G. Chu, J. Sun and C. Chen, *J. Power Sources*, 2012, **208**, 210–224.
- 41 C. H. Doh, D. H. Kim, H. S. Kim, H. M. Shin, Y. D. Jeong, S. I. Moon, B. S. Jin, S. W. Eom, H. S. Kim, K. W. Kim, D. H. Oh and A. Veluchamy, *J. Power Sources*, 2008, **175**, 881–885.
- 42 J. Lamb, C. J. Orendorff, L. A. M. Steele and S. W. Spangler, *J. Power Sources*, 2015, **283**, 517–523.
- 43 K. Saravanan, C. W. Mason, A. Rudola, K. H. Wong and P. Balaya, *Adv. Energy Mater.*, 2013, **3**, 444–450.
- 44 Z. Jian, W. Han, X. Lu, H. Yang, Y. Hu, J. Zhou, Z. Zhou, J. Li, W. Chen, D. Chen and L. Chen, *Adv. Energy Mater.*, 2013, **3**, 156–160.
- 45 Y. Fang, L. Xiao, X. Ai, Y. Cao and H. Yang, *Adv. Mater.*, 2015, **27**, 5895–5900.
- 46 Y. Li, R. Huang, G. Pan, J. Yao and Z. Zou, *ACS Omega*, 2019, **4**, 7759–7765.
- 47 T. Wei, G. Yang and C. Wang, *Nano Energy*, 2017, **39**, 363–370.
- 48 Q. Zhang, P. Man, B. He, C. Li, Q. Li, Z. Pan, Z. Wang, J. Yang, Z. Wang, Z. Zhou, X. Lu, Z. Niu, Y. Yao and L. Wei, *Nano Energy*, 2020, **67**, 104212.
- 49 G. Wang, Y. Zhang, B. Guo, L. Tang, G. Xu, Y. Zhang, M. Wu, H. Liu, S. Dou and C. Wu, *Nano Lett.*, 2020, **20**, 4464–4471.
- 50 Y. Cheng, S. Wang, L. Zhou, L. Chang, W. Liu, D. Yin, Z. Yi and L. Wang, *Small*, 2020, **16**, 2000681.
- 51 P. Xiong, R. Ma, N. Sakai, L. Nurdiwijayanto and T. Sasaki, *ACS Energy Lett.*, 2018, **3**, 997–1005.